RESEARCH PAPER

A New Post-hoc Flat Field Measurement Method for the Solar X-Ray and Extreme Ultraviolet Imager Onboard the FengYun-3E Satellite

View the article online for updates and enhancements.

CrossMark

A New Post-hoc Flat Field Measurement Method for the Solar X-Ray and Extreme Ultraviolet Imager Onboard the FengYun-3E Satellite

Qiao Song[1,2,3] , Xianyong Bai[4,*], Bo Chen[5,*], Xiuqing Hu[3,6,*], Yajie Chen[7], Zhenyong Hou[7], Xiaofan Zhang[4], Lingping He[5], Kefei Song[5], Peng Zhang[3,6], Jing-Song Wang[1,3], Xiaoxin Zhang[1,3], Weiguo Zong[1,3], Jinping Dun[1,3], Hui Tian[7], and Yuanyong Deng[4]

[1] Key Laboratory of Space Weather, National Satellite Meteorological Center (National Center for Space Weather), China Meteorological Administration, Beijing 100081, China
[2] State Key Laboratory of Space Weather, Chinese Academy of Sciences, Beijing 100190, China
[3] Innovation Center for Fengyun Meteorological Satellite, China Meteorological Administration, Beijing 100081, China; huxq@cma.gov.cn
[4] National Astronomical Observatories, Chinese Academy of Sciences, Beijing 100101, China; xybai@bao.ac.cn
[5] Changchun Institute of Optics, Fine Mechanics and Physics, Chinese Academy of Sciences, Changchun 130033, China; chenb@ciomp.ac.cn
[6] Key Laboratory of Radiometric Calibration and Validation for Environmental Satellites, National Satellite Meteorological Center (National Center for Space Weather), China Meteorological Administration, Beijing 100081, China
[7] School of Earth and Space Sciences, Peking University, Beijing 100871, China

Abstract

Extreme ultraviolet (EUV) observations are widely used in solar activity research and space weather forecasting since they can observe both the solar eruptions and the source regions of the solar wind. Flat field processing is indispensable to remove the instrumental non-uniformity of a solar EUV imager in producing high-quality scientific data from original observed data. FengYun-3E (FY-3E) is a meteorological satellite operated in a Sun-synchronous orbit, and the routine EUV imaging data from the Solar X-ray and Extreme Ultraviolet Imager (X-EUVI) onboard FY-3E has the characteristic of concentric rotation. Taking advantage of the concentric rotation, we propose a post-hoc flat field measurement method for its EUV 195 Å channel in this paper. This method removes the small-scale and time-varying component of coronal activities by taking the median value for each pixel along the time axis of a concentric rotation data cube, and then derives the large-scale and invariable component of the quiet coronal radiation, and finally generates a flat field image. The flat field can be generated with cadences from hundreds of minutes (one orbit) to several days. Higher flat field accuracy can be achieved by employing more data. Further analysis shows that our method is able to measure the instrumental spot-like non-uniformity possibly caused by contamination on the detector, which mostly disappears after the in-orbit self-cleaning process. It can also measure the quasi-periodic grid-like non-uniformity, possibly from the obscuration of the support mesh on the rear filter. After flat field correction, these instrumental non-uniformities from the original data are effectively removed. Moreover, the X-EUVI 195 Å data after dark and flat field corrections are consistent with the 193 Å imaging data from the Atmospheric Imaging Assembly onboard the Solar Dynamics Observatory, verifying the suitability of the method. The post-hoc method does not occupy observation time, which is advantageous for space weather operations. Our method is not only suitable for FY-3E/X-EUVI but also a candidate method for the flat field measurement of future solar EUV telescopes.

Key words: Sun: corona – techniques: image processing – methods: data analysis – methods: observational

1. Introduction

Space weather is important to satellites, spacecraft and astronauts as human exploration expands from our home planet Earth to the Moon, Mars, and beyond. The expansion of technological infrastructure on Earth also highlights the impact of space weather. The primary driver of space weather is the Sun (Schwenn 2006). Its highly dynamic atmosphere produces various activities such as solar flares and coronal mass ejections. In the extreme ultraviolet (EUV) wavelengths, almost all solar activities in the outer layers of the solar atmosphere (i.e., the chromosphere, the transition region, and the corona) can be observed. Solar active regions usually show bright loop systems in EUV images, and with the evolution of the magnetic field in active regions, the loop systems of the active regions also change dynamically. When a flare occurs, the source region can be identified from EUV images, and then the flare process can be tracked and studied (Song et al. 2022). In EUV images, coronal holes are also observed, which are cooler, less dense regions in the solar atmosphere. Coronal

holes are generally believed to be the source of the solar wind that can cause geomagnetic storms and other space weather disturbances (Pulkkinen 2007). Other solar activities, such as EUV waves (Hou et al. 2022) and filament eruptions can also be well represented on EUV images. Moreover, the variability of solar EUV radiation influences Earth's atmosphere and further climate on different timescales. On the short timescale, major solar flares can affect Earth's ionosphere, causing disturbances such as blackout of high-frequency radio communication and degradation of low-frequency navigation signals. Solar influence on Earth's climate is often reflected in the radiation changes of EUV and other wavelengths on the 11 yr period of solar cycles (Lockwood 2012).

Therefore, EUV wavelengths are widely considered in solar activity research and space weather forecasting. Due to the absorption of Earth's atmosphere, solar EUV telescopes need to be onboard a satellite or spacecraft. Examples include the Transition Region and Coronal Explorer (TRACE, Handy et al. 1999), Extreme ultraviolet Imaging Telescope (EIT, Delaboudinière et al. 1995) for the SOHO Mission, the Sun Earth Connection Coronal and Heliospheric Investigation (SECCHI, Howard et al. 2008) on the twin STEREO spacecraft, the Sun Watcher using Active pixel system detector and image Processing (SWAP, Halain et al. 2013) telescope on the PROBA2 technological mission, the Atmospheric Imaging Assembly (AIA, Lemen et al. 2012; Boerner et al. 2012) on the Solar Dynamics Observatory (SDO, Pesnell et al. 2012), and the Solar X-ray and Extreme Ultraviolet Imager (X-EUVI, Chen et al. 2022a, 2022b) onboard the FengYun-3E (FY-3E, Zhang et al. 2022) satellite. FY-3E is the latest one of China's second generation polar-orbiting meteorological satellites. Launched on 2021 July 5, FY-3E is now operating in a Sun-synchronous orbit (i.e., dawn/dusk orbit) at ∼836 km altitude with an inclination of 98°.75. The X-EUVI has multiple X-ray and EUV channels that can be used for space weather forecasting and scientific research. In its EUV wavelength, it provides full-disk 195 Å images of the Sun with a moderate spatial resolution (∼2″.5 per pixel) and a high time resolution up to a few seconds. In addition, the solar images of X-EUVI can be combined with images from the Advanced Space-based Solar Observatory (ASO-S, Gan et al. 2019) and the Chinese Hα Solar Explorer (CHASE, Li et al. 2022) mission for multi-band comprehensive observations to study solar activities.

Due to large-scale vignetting in the optical system, the small-scale pixel-to-pixel variation of the charge-coupled device (CCD) detector and the unavoidable intermediate-scale contamination or dust from the optical elements and the CCD detector, the recorded data from all of the EUV solar telescopes are non-uniform even if the target is a light source with uniform light emitting area. In addition, the nickel mesh supporting the focal-plane filter can also create grid-like features on the observed image, resulting in increased non-uniformity (Boerner et al. 2012; Seaton et al. 2013). Therefore, flat field processing is generally employed to remove the non-uniformity of the whole system in the production of high-quality scientific data from original observed data. However, up to now, how to acquire a precise flat field image is still one of the most challenging problems for full-disk solar observations. The best and easiest way to measure the instrumental flat field is to find a highly uniform light source (Howard et al. 2008; Kentischer et al. 2008; Bai et al. 2017; Wang et al. 2019), which is extremely difficult at the EUV wavelength. An alternative way is to adopt a non-uniform light source such as the Sun itself and the flat field is generated by taking several offset solar images with slightly shifted locations on the detector. The offset can be realized by changing the tip-tilt angles of the second mirror. It can also be taken by changing the pointing of the spacecraft. Both of these methods are used for flat field measurement of the EUV imagers of the Sun, e.g., TRACE and SDO/AIA. Once a series of offset images is taken, the shifts in the x and y directions relative to the reference image are determined and then the flat field is generated by the Kuhn-Lin algorithm (Kuhn et al. 1991). Other algorithms were also proposed to derive flat field (Chae 2004; Xu et al. 2016; Gao et al. 2020; Li et al. 2021).

If the offset solar images have acentric rotation on the detector due to the attitude control of a spacecraft, there are both rotation and shift during the image registration process, making it difficult to employ the above-mentioned methods to generate the flat field. In this paper, we propose a new post-hoc method to create flat fields from the routine concentric rotated coronal images taken by FY-3E/X-EUVI. A similar method has been used for the generation of flat field and polarized offset from regular observed full-disk photospheric filtergrams and Stokes $\frac{Q}{I}$, $\frac{U}{I}$, $\frac{V}{I}$ maps, respectively (Potts and Diver 2008; Wachter and Schou 2009; Bai et al. 2018). Here we extend it to regular observational data of the corona. The principle of our method is presented in Section 2. Section 3 shows the results of the method application in observational images, followed by a conclusion and discussion section (Section 4).

2. Principle of the Post-hoc Flat Field Measurement Method

The recorded image $I(x,y)$ taken by a solar EUV telescope can be expressed as

$$I(x, y) = I_s(x, y) \times f(x, y) + I_d, \qquad (1)$$

where $I_s(x,y)$, $f(x,y)$ and I_d represent the solar-disk coronal radiation maps, flat field and dark field of the whole system, respectively. From Equation (1), the solar-disk radiation $I_s(x,y)$ can be recovered from the original recorded data $I(x,y)$ once the flat field and dark field are obtained. The key step is to measure the flat field and dark field. If we try to divide the solar-disk coronal radiation into two parts, $I_s(x,y)$ becomes

$$I_s(x, y) = I_s^l(x, y) + I_s^h(x, y). \qquad (2)$$

Here $I_s^l(x, y)$ corresponds to the large-scale component, that is to say the quiet coronal radiation with limb brightening pattern caused by the optically thin effect of EUV lines (Withbroe 1970), which rarely changes with time (i.e., with low frequency in time variation). $I_s^h(x, y)$ represents the time-varying medium and small-scale components, such as the active region loops, the coronal holes, and the coronal bright points (i.e., with high frequency in time variation).

If a series of EUV coronal radiation maps $I_s(x, y, t)$ having concentric rotation within several days is used to create a data cube and the median value is taken for each spatial pixel, the time-varying component $[I_s^h(x, y, t)]_{\text{median}} \approx 0$ while the large-scale component remains almost the same. Then Equation (2) can be written as

$$
\begin{aligned}
[I_s(x, y, t)]_{\text{median}} &\approx [I_s^l(x, y, t)]_{\text{median}} \\
&+ [I_s^h(x, y, t)]_{\text{median}} = I_s^l(x, y).
\end{aligned}
\tag{3}
$$

Once the non-uniformity of the $I_s^l(x, y)$ is known, we can divide it by the $[I_s(x, y, t)]_{\text{median}}$ image and the final image can be treated as a uniform light source used for flat field measurement. According to Equation (1), the flat field is calculated from the median of dark-corrected routine EUV coronal images with

$$
f(x, y) = \frac{[I(x, y, t) - I_d]_{\text{median}}}{I_s^l(x, y)}.
\tag{4}
$$

Now the main task is to calculate the the large-scale components $I_s^l(x, y)$, which have circular symmetry in general since what we observe is a projection of the spherical coronal radiation. It is more convenient to make a conversion of coordinates from a Cartesian lattice to polar coordinates to deal with the circular symmetry.

$$
I'(r, \theta) = I'(x, y) = [I(x, y, t) - I_d]_{\text{median}}.
\tag{5}
$$

The r and θ in Equation (5) are the radius and azimuth angles, respectively, and $I'(r, \theta)$ is the median of a series of dark-corrected routine coronal images in polar coordinates. If we take the median value for the intensities along all of the azimuth angles with the same radius, the quiet coronal radiation and limb brightening curve can be derived, which is described in the equation below

$$
I'(r) = I'(r, \theta)|_{\text{median along } \theta \text{ direction}}.
\tag{6}
$$

We are able to further obtain the large-scale coronal component $I_s^l(x, y)$ by filling in the values in the azimuth direction for each radius with the values in Equation (6) and transforming it back to Cartesian coordinates. Finally, the flat field is generated from Equation (4), and the flat field corrected corona radiation is derived with Equation (1).

3. Results

We use the EUV coronal images from the FY-3E/X-EUVI 195 Å channel to test the performance of the method. Since FY-3E is a polar-orbiting meteorological satellite, its main pointing is Earth and its observational images of the Sun have significant rotation. The X-EUVI has a two-dimensional turntable to point and track the Sun. It is also equipped with an imaging stabilization system to rapidly compensate the jitters from the satellite and a turntable to improve the spatial resolution. The routine coronal images rotate with the orbital period of ~101.5 minutes, which is concentric with the help of the imaging stabilization system. If we create a data cube from the stacked concentric rotated images taken within one orbit and take the median values for each spatial pixel, the assumption is that $I_s^h(x, y) \approx 0$ still works. Then we can employ the method in Section 2 to derive the flat field.

3.1. Flat Field Generated from X-EUVI's Data

Figure 1 displays the time series of the EUV 195 Å images observed in the first orbit on 2021 October 29, with an interval of about 20 minutes between each panel of the figure. The exposure time of each image is 0.8 second and the dark field has been corrected. The dark field of X-EUVI is taken in the calibration mode with the same time as a normal exposure, but with the shutter closed, and the telescope is pointed in the same way as a normal observation, so as to ensure that the dark field and solar observation images have the same temperature conditions on the telescope and the CCD detector. As can be seen from the figure, there is a polar coronal hole near the north pole of the Sun. The arrows in the figure indicate the changing north pole direction, and the dashed lines signify the initial position of concentric image rotation. The horizontal and vertical coordinates of the image are pixels. As the satellite orbits the Earth, the solar image rotates counterclockwise at an angular velocity of about 3.5° per minute. At 01:05 UT, the coronal hole is located at the lower right of the image (Figure 1(d)), and it turns counterclockwise to the upper position of the image (Figure 1(e)) at 01:46 UT. Finally, after the image is rotated nearly 360°, the coronal hole switches back to the lower right of the image again at 02:46 UT (Figure 1(f)).

With the first orbit data on 2021 October 29 shown in Figure 1, we derived the flat field using the method described in Section 2 and the result is presented in Figure 2. Figure 2(a) is the $[I(x, y, t) - I_d]_{\text{median}}$ image in the Cartesian coordinate system obtained by the median value of each pixel from a time series of 417 frames. After the processing, the small-scale components of the coronal radiation $I_s^h(x, y)$ are almost eliminated. From the image, we can see the residual large-scale coronal component $I_s^l(x, y)$, i.e., the quiet radiation with circular symmetry and the limb brightening pattern. We can also see the instrumental non-uniformity, i.e., the spot-like
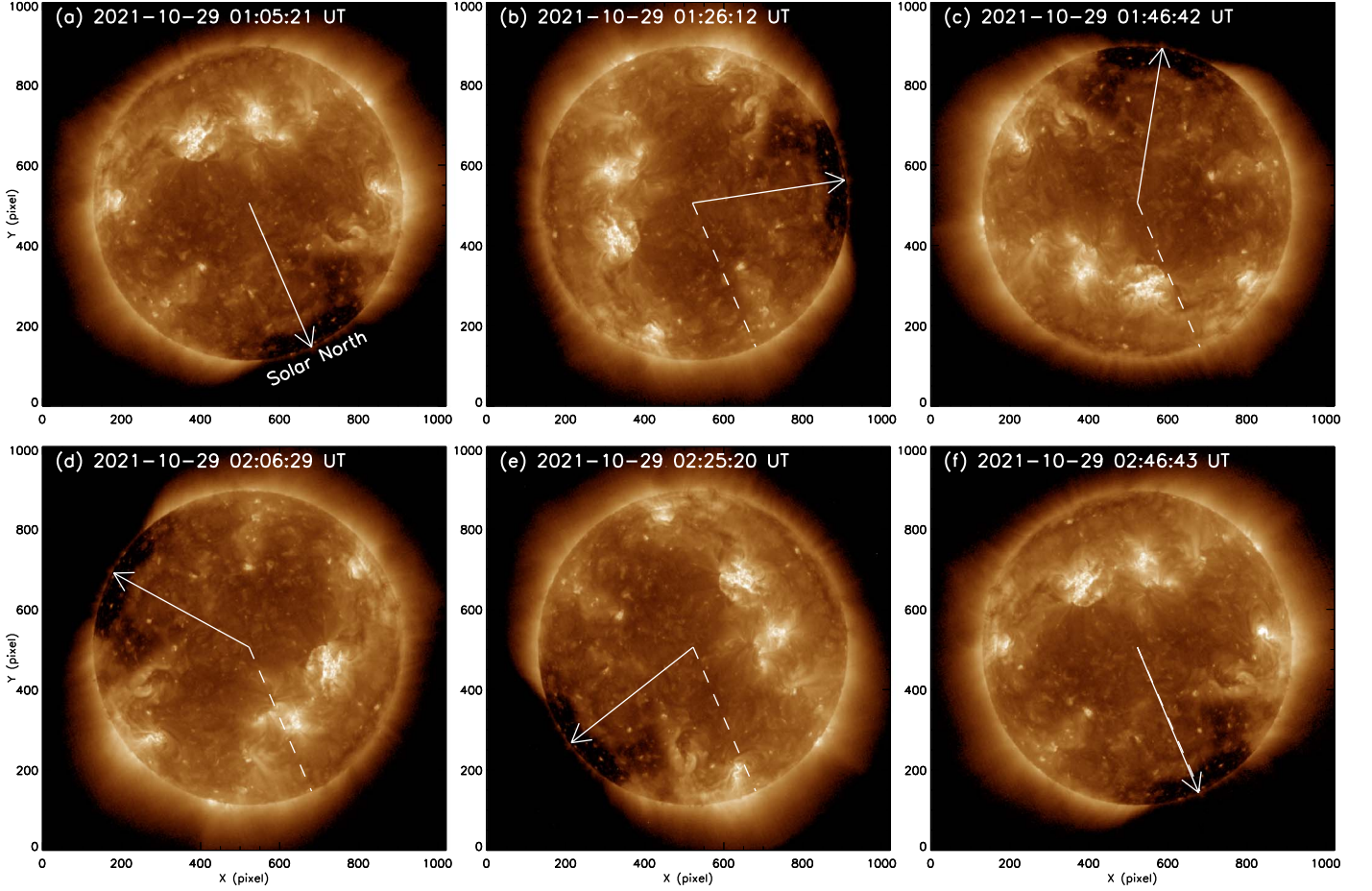
Figure 1. Time series of the X-EUVI 195 Å images within one orbit showing counterclockwise rotation. The arrows in the figure indicate the north pole direction of the Sun, and the dashed lines signify the initial position.

features and quasi-periodic grid-like features. Figure 2(b) is the median $I'(r)$ curve calculated from Equation (6) after transforming Figure 2(a) to polar coordinates with Equation (5). Since solar active regions and other active features have been smoothed out, we can see the quiet coronal radiation from the solar disk and bright solar limb. Figure 2(c) displays the quiet coronal radiation $I_s^l(x, y)$ image derived from Figure 2(b), and it can be seen that only bright limb and concentric circle features remain on this image. Figure 2(d) is the final flat field image obtained according to Equation (4). At this time, there is mostly instrumental non-uniformity left, such as the grid-like features and some inhomogeneous intermediate-scale features.

In Figure 2, the flat field is generated with a data cube in one orbital period. The accuracy of the flat field depends on the elimination of small-scale components of the corona $I_s^h(x, y)$. The discussion from Potts and Diver (2008) and Bai et al. (2018) indicates that the accuracy of the generated flat field is directly proportional to $\frac{\delta I}{\sqrt{n}}$, where n is the number of employed images and δI is the fluctuation of radiation among various

coronal features. Small δI is satisfied by choosing the observed EUV images with less coronal hole or solar active regions. Moreover, more EUV images with larger n help to improve the accuracy, which is confirmed in Figure 3. Figures 3(a) and (b) is flat field images produced using one-day's data of 2021 July 22 and 2021 October 29, respectively. These two sets of data represent two typical instrumental non-uniformities of the X-EUVI 195 Å channel. Obscuration of the Earth and the satellite itself, as well as multi-channel observation modes, can reduce the number of available EUV images in one orbit for the flat field processing, and then affect the accuracy of the flat field image. Therefore, the available EUV images in 2021 October 29 are more than twice those of the data on 2021 July 22, which result in a better flat field accuracy in October 2021. Figures 3(b) and (c) is the flat field images generated from the data from one day on October 29 (5894 frames) and two days on October 29–30 (11928 frames), respectively. Comparing Figure 2(d) with Figures 3(b) and (c), the residual inhomogeneity of the time-varying component $I_s^h(x, y)$ is found in the flat field using single-orbit data in Figure 2(d). With the
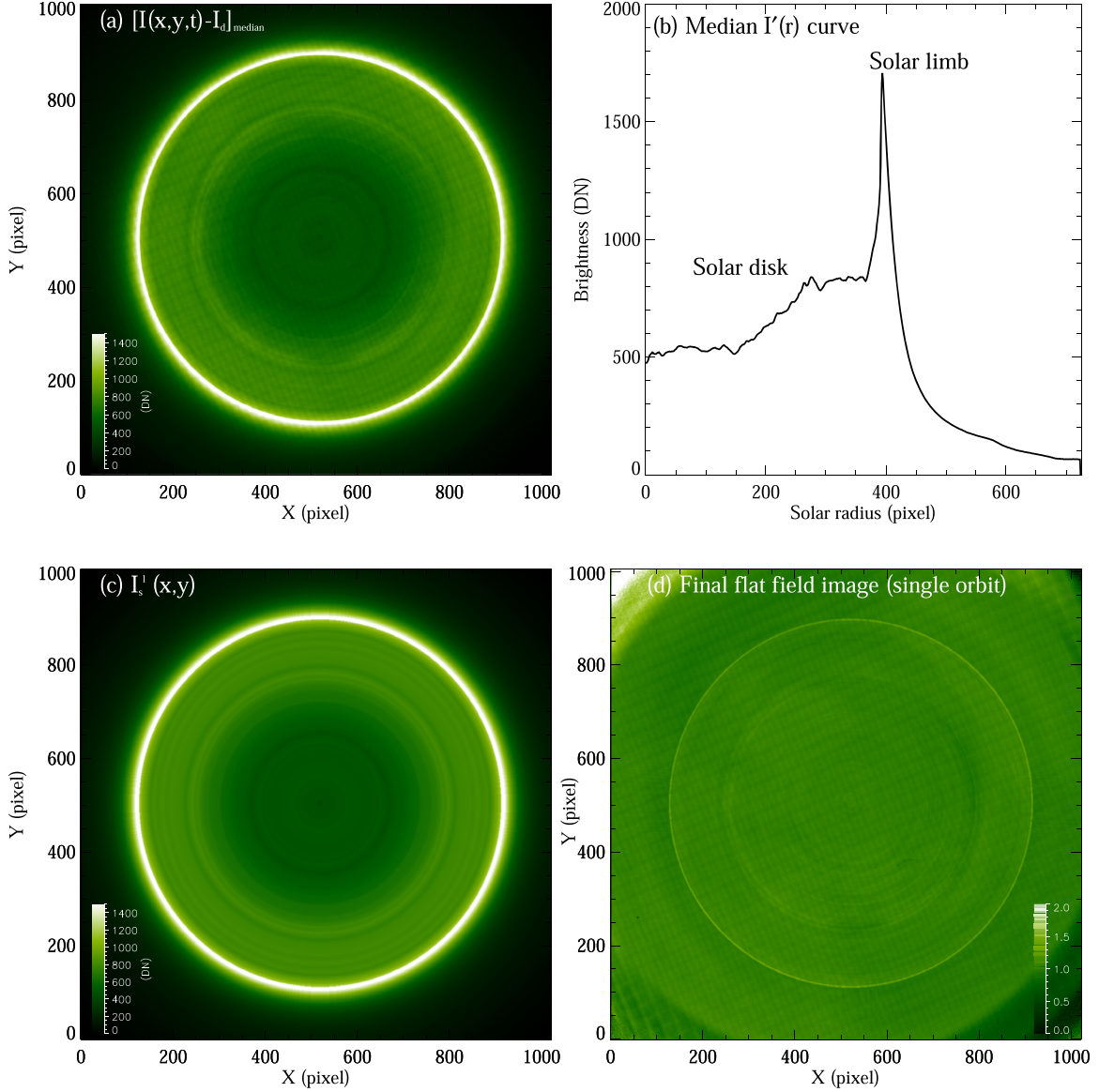
Figure 2. Calculation and generation process of the flat field image. (a) The dark corrected median data $[I(x, y, t) - I_d]_{\mathrm{median}}$ from time series images of the first orbit on 2021 October 29, and (b) features the median $I'(r)$ curve representing the quiet coronal radiation derived from (a). (c) The quiet coronal radiation $I_s^l(x, y)$ image derived from (b), and (d) is the final flat field image of the time series data in Cartesian coordinates.

increasing number of frames n, the residual solar-disk features on the flat field images become less and less. From the flat field using three days of routine EUV images (October 29–31, with 17948 frames) shown in Figure 3(d), the residual solar features basically disappear, and the grids and spot-like features are more prominent. The arc-shaped pattern (see the red arrows) in the right part of Figures 3(a) and (c) is possibly caused by the vignetting effect from the optical system of the instrument. It should be pointed out that the errors at the edge of the flat field image, especially at the four corners, may be large, due to the small number of data pixels there.

3.2. Evaluation of the Flat Field Processing

With the flat field calculated from one day of data, we carried out the flat field processing of the original EUV 195 Å images according to Equation (1) for two days in July 2021 and October 2021, respectively. The results are arranged in Figures 4 and 5. Figures 4(a1) and (a2) is the original full-disk data and the calibrated image after dark and flat field corrections, respectively. Figures 5(a1) and (a2) is for a local region in order to better show the improvement after the correction of instrumental non-uniformity. On July 22, X-EUVI's self-cleaning mode was about to start, and there
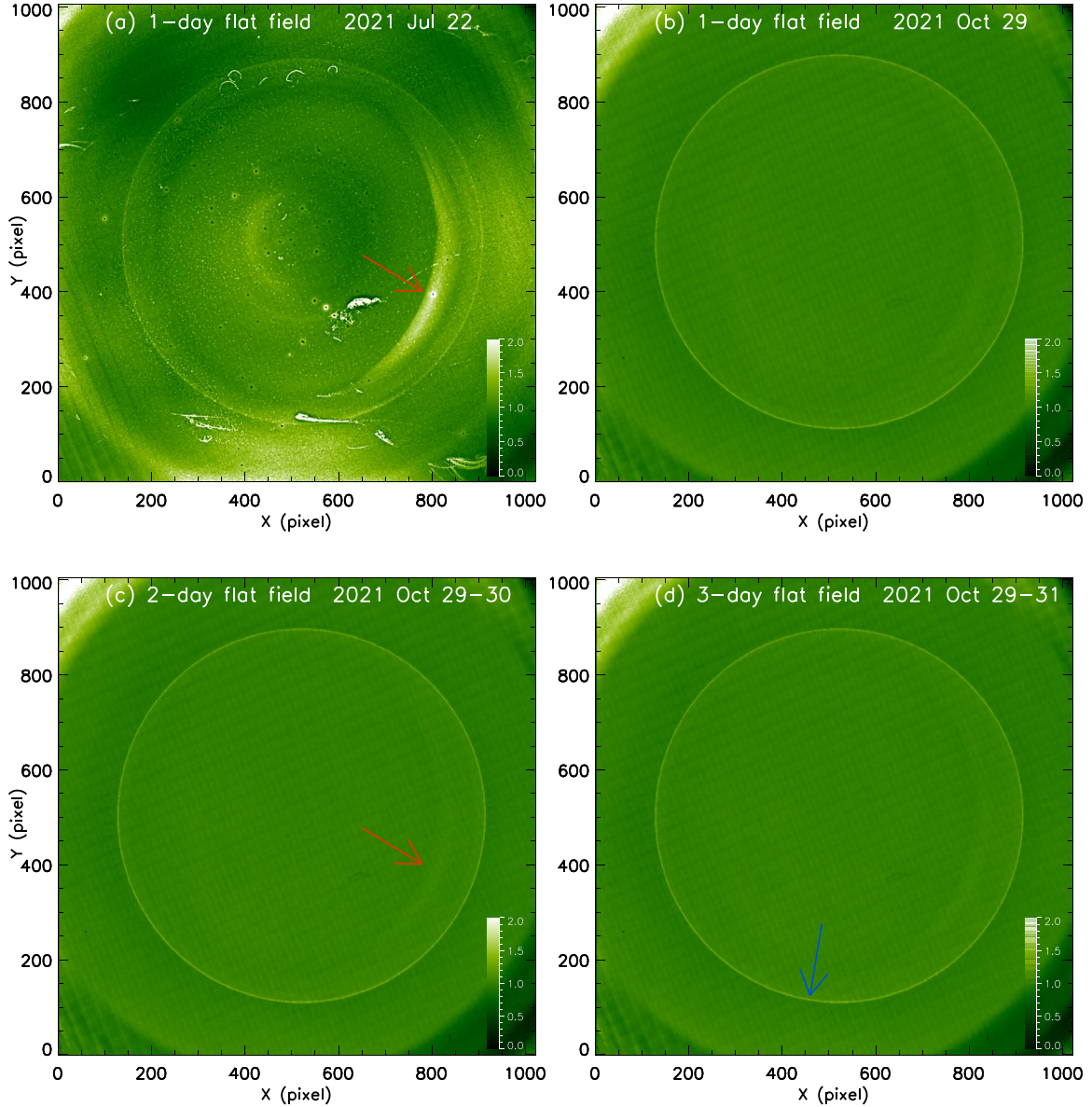
Figure 3. Flat field images of one-day, two-day and three-day data. The red arrows in (a) and (c) indicate the arc-shaped pattern that is possibly caused by the vignetting effect from the optical system. The blue arrow in (d) shows the narrow ring at the solar limb which is possibly caused by limited instrument pointing accuracy and stability.

are multiple spot-like features on the image (see Figure 4(a1)) possibly caused by the adsorbed contaminant on the CCD detector. It can be seen that these spot-like features basically disappear after the flat field correction (Figure 4(a2)). In Figure 5(a1), we extracted one line (Cut1) at $x = 150$ with a spot-like feature from $y = 115$ to $y = 145$. From the flat field at the positions of Cut1 marked by the blue dot–dashed line in Figure 5(a3), the normalized values in the spot-like features are in the range of 0.5 to 3. The coronal bright point (see the arrow in Figure 5(a2) and the red dashed line in Figure 5(a3)), which is hardly found at the position of the spot-like feature, is clearly

seen after the flat field correction. According to the flat field data, the contamination on the detector on 2021 July 22 is the most serious so far, and the successful correction of heavily contaminated images demonstrates the effectiveness of our method.

Figures 4(b1) and (b2) is the original and corrected images on 2021 October 28, respectively. A self-cleaning of the instrument had just been completed on this day, so there are no obvious spot-like features from the deposited contaminant. From the flat field derived from one day's concentric rotation data in Figure 3(b) on October 29, we can also confirm that the
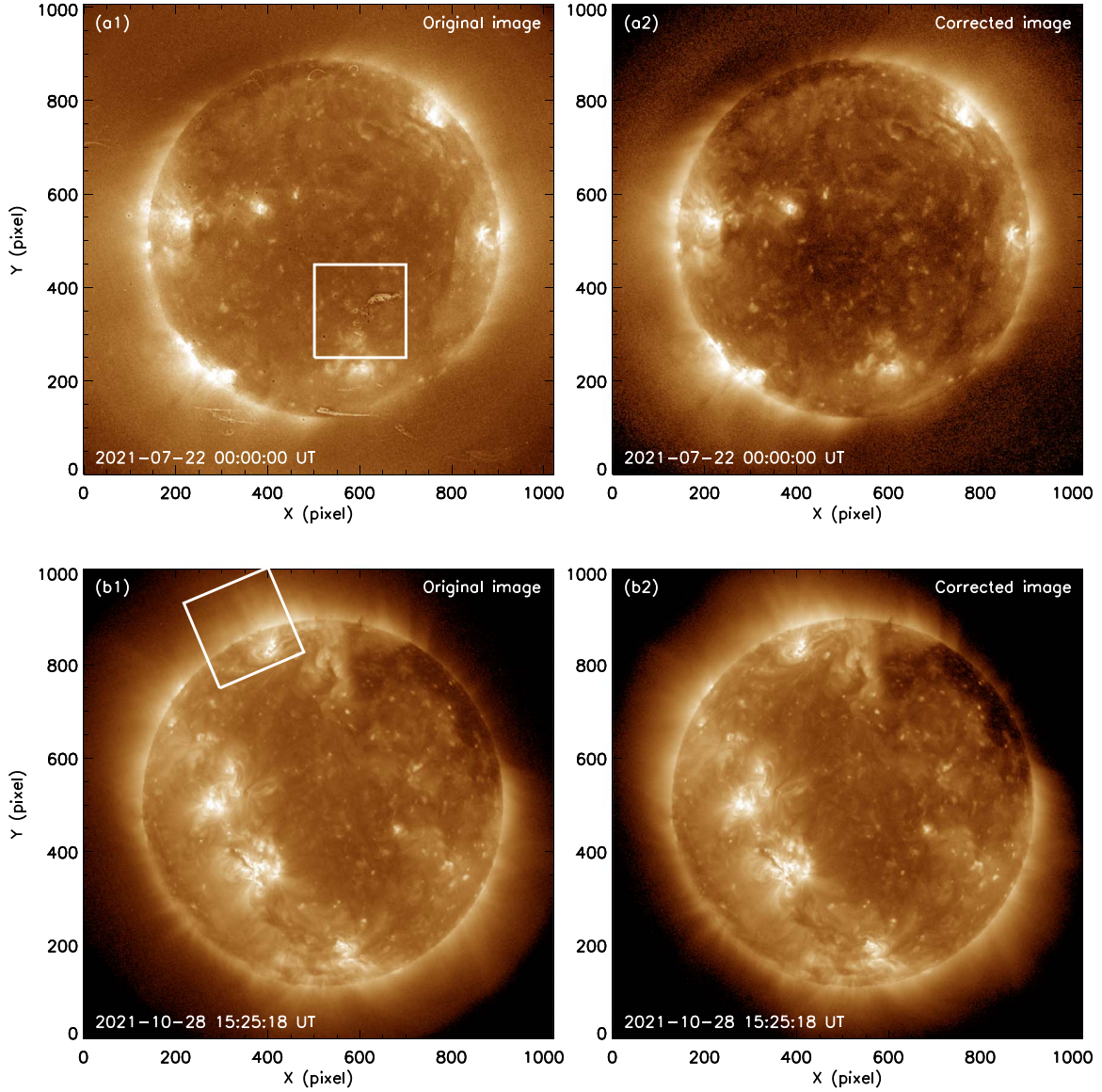
Figure 4. The solar full-disk images before (left column) and after (right column) the flat field processing for 2021 July 22 (upper row) and October 28 (bottom row). The boxes in (a1) and (b1) represent the field of view of Figures 5(a1) and (b1), respectively.

instrumental non-uniformity from the contaminant is non-significant. It indicates that the self-cleaning mode of X-EUVI is quite efficient to reduce the non-uniformity caused by the contaminant. After self-cleaning, the most obvious instrumental non-uniformity is the small grid-like features caused by the differential obscuration from the support mesh of the X-EUVI's focal-plane filter (i.e., the rear filter) seen in Figure 3(b). The support mesh is installed at a distance of 16.7 mm from the CCD detector, with a grid period of 363 μm and a grid width of 30 μm. In Figure 5(b1), we mark the positions of two grid-like features with arrows. The grids become vertical after we rotate the images in Figure 4(b1) counterclockwise with an angle of 67°. A local region near the solar limb (see the box in

Figure 4(b1)) is selected and is shown in Figure 5(b1), and Figure (b2) is the same region after the flat field correction. Comparing the two images before and after flat field correction, the grid-like features almost disappear (Figures 4(b2) and 5(b2)). A horizontal line in Figure 5(b1) is selected for a slice of Cut2. The original, flat field and flat field corrected values in the line are presented in Figure 5(b3). From the blue dot–dashed flat field values, the grid-like features have fluctuation with an amplitude of 14% (from 0.91 to 1.05) and a period of about 30 pixels. The pixel size of the CCD detector of X-EUVI is 13 μm, so the period of the grid-like features is about 390 μm, which does not exactly equal the period of the support mesh. However, considering the mesh is located at a distance
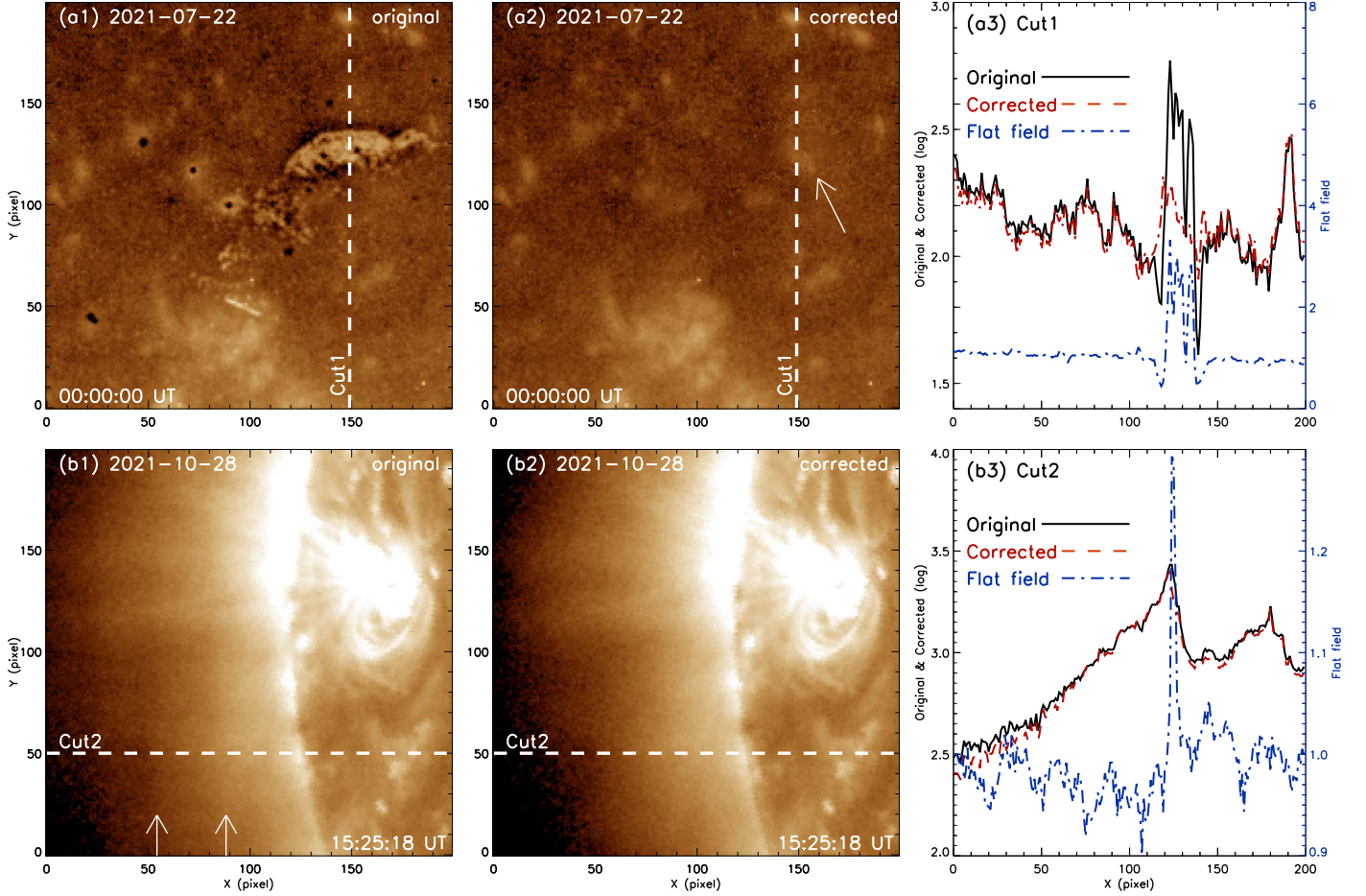
Figure 5. The local region from Figure 4 before (left column) and after (middle column) the flat field processing. The solid, red dashed, and blue dot–dashed lines in the right column correspond to the original intensity, the intensity after flat field processing, and the values used in the flat field extracted from the dashed lines (i.e., Cut1 and Cut2) in the left and middle columns respectively. The arrow in (a2) indicates a coronal bright point that was revealed after the flat field processing. The two arrows in (b1) mark the positions of two quasi-periodic grid-like features.

of 16.7 mm from the CCD detector, the result is reasonable. Due to the low amplitude of the grid-like features and the large dynamic range of coronal features, the visual effect of the flat field processing is not as significant as that for the spot-like features. However, the images show that the radial structures in the corona, such as coronal plumes and coronal streamers, are clearer after the flat field correction. Therefore, we believe that the flat field processing greatly improves the quality of the EUV images for the coronal radiation observation of X-EUVI.

After dark and flat field corrections with our method, the comparative analysis results show that the X-EUVI 195 Å coronal radiation is consistent with that from the SDO/AIA 193 Å channel. Figure 6(a1) is an X-EUVI 195 Å image at 09:11 UT on 2021 October 28, and Figure 6(a2) is an almost simultaneous AIA 193 Å image for comparison. The X-EUVI image has been aligned with the AIA image by the image registration process that includes image scale correction, and

shift and rotation corrections using the cross-correlation method manually. It can be seen that the coronal features of the X-EUVI image on both solar disk and solar limb agree well with those of the AIA image. We take horizontal and vertical slices on the images, where Cut3 is parallel to the solar Y-axis, and Cut4 is parallel to the solar X-axis. Figure 6(b1) depicts the brightness variation along Cut3, and features such as coronal bright points, active region loops, and a dark region corresponding to a coronal hole can be seen in this light curve. We normalized the brightness curve to facilitate comparative analysis, where the black line represents X-EUVI 195 Å images and the red dotted line corresponds to AIA 193 Å data. The brightness variation along Cut4 shows a limb brightening pattern in the EUV wavelength (see Figure 6(b2)). Although the curves of the AIA 193 Å channel are sharper at the coronal loops, the bright points, solar limb, and other small-scale features, because of their higher spatial resolution ($0\rlap{.}''6$ per pixel), the overall
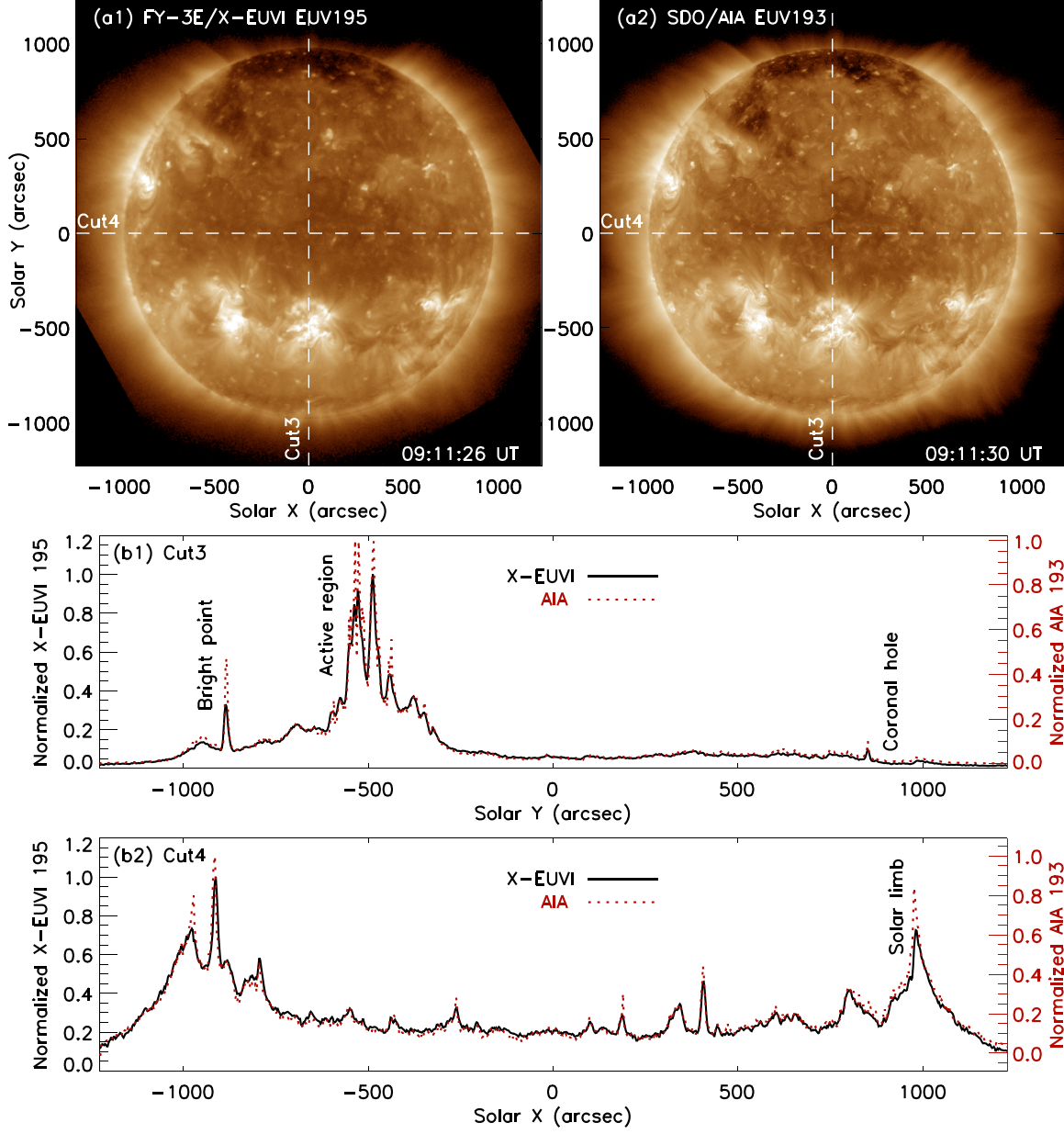
Figure 6. Comparison of X-EUVI 195 Å and SDO/AIA 193 Å images on 2021 October 28. Cut3 is parallel to the solar *Y*-axis, and Cut4 is parallel to the solar *X*-axis. In (b1) and (b2), the black line represents X-EUVI 195 Å and the red dotted line corresponds to AIA 193 Å light curves with normalized brightness.

trends of FY-3E/X-EUVI 195 Å and SDO/AIA 193 Å light curves are consistent across the entire solar disk.

4. Conclusion and Discussion

The routine EUV 195 Å imaging data from FY-3E/X-EUVI have imaging rotation with a speed of 3.5° per minute. If several offset solar images taken by changing the satellite's pointing are used to derive the flat field, it will be very difficult because there are both rotation and shift during the image registration process. In the paper, we proposed a new post-hoc

flat field measurement method taking advantage of the concentric rotation property in the routine data taken with the imaging stabilization system of the X-EUVI. An advantage of the post-hoc method is that it does not need to occupy the observation time for calibration of the flat field, which can facilitate convenient and continuous observations, and this is valuable for space weather operations.

The principle of our method is that the small-scale and time-varying component of the coronal radiation is approximately zero if we make a data cube from plenty of concentric rotation images and take the median value for each pixel along the time

axis. The large-scale and invariable component can further be derived assuming that it is symmetrical under all rotations about the center of the solar disk. Once the large-scale and invariable coronal radiation is removed, the remaining part is the flat field. For the X-EUVI's routine EUV 195 Å imaging data, the flat field can be generated with cadences from hundreds of minutes (one orbit) to several days. The accuracy of the flat field depends on how much coronal radiation is left with the limited data and the processing method. In the paper, the flat field is derived with the period of one orbit, and one, two and three days. From the comparison, it is found that higher flat field accuracy can be achieved by employing more data. Obviously if more data (larger n) are used, it takes more time to generate a flat field. Once the instrumental flat field changes during this period, we merely obtain the averaged flat field. From the comparison of Figures 3(a) and (b), our method can monitor the changes in the flat field image due to the contamination on the CCD detector and other reasons, and thus it can support routine calibration. It provides a convenient flat field calibration option for observation instruments that are difficult to maintain manually, such as space-based instruments and automatic observatories located in remote areas. The signal to noise ratio from the original imaging data is not included in the derivation of flat field in Section 2, which is discussed in Potts and Diver (2008) and Bai et al. (2018) and is the same for coronal observations.

The flat field from 2021 July 22 affirms that the new method is able to measure the instrumental spot-like non-uniformity possibly from the contamination on the detector, which mostly disappears after the in-orbit self-cleaning process seen from what is taken on October 29 (see Figures 3(a) and (b)). The dramatic change in the flat field images before and after the self-cleaning process also demonstrates the effectiveness of the self-cleaning mode of the X-EUVI. Furthermore, the quasi-periodic grid-like non-uniformity possibly from the obscuration of the support mesh on the rear filter can also be obtained from the flat field, which has fluctuation with a small amplitude and a period of about 30 pixels, and it is roughly in line with the parameters of the support mesh. After the flat field correction, the instrumental non-uniformity from the original data is effectively removed. The narrow and bright ring at the solar limb in the flat field image (see the blue arrow in Figure 3(d)) is possibly caused by limited instrument pointing accuracy and stability, which can lead to sub-pixel drift in the position of the center of the solar disk, and sometimes results in slight asymmetry in the derived median image with Equation (4). It may also be caused by the limited accuracy of the derived solar disk center. In future works, we will try to remove the influence of the ring and study the changes of the flat field on different timescales. To better illustrate the availability of our flat field method, we compare the X-EUVI 195 Å data after dark and flat

field corrections with the 193 Å imaging data from SDO/AIA. We find that they are consistent with each other except that AIA has higher spatial resolution. Overall, we provide a candidate method for the flat field measurement of current and future solar EUV telescopes.

ORCID iDs

Qiao Song ⓘ https://orcid.org/0000-0003-3568-445X

References

Bai, X., Deng, Y., Wang, Y., Liu, S., & Mao, X. 2018, ChSBu, 63, 302
Bai, X., Wang, Y., Zhang, Z., et al. 2017, AcOpS, 37, 0523002
Boerner, P., Edwards, C., Lemen, J., et al. 2012, SoPh, 275, 41
Chae, J. 2004, SoPh, 221, 15
Chen, B., Ding, G.-X., & He, L.-P. 2022a, Light Sci Appl, 11, 29
Chen, B., Zhang, X., He, L., et al. 2022b, Under review
Delaboudinière, J. P., Artzner, G. E., Brunaud, J., et al. 1995, SoPh, 162, 291
Gan, W.-Q., Zhu, C., Deng, Y.-Y., et al. 2019, RAA, 19, 156
Gao, X., Chen, B., He, L., & Zheng, X. 2020, SoPh, 295, 12
Halain, J. P., Berghmans, D., Seaton, D. B., et al. 2013, SoPh, 286, 67
Handy, B. N., Acton, L. W., Kankelborg, C. C., et al. 1999, SoPh, 187, 229
Hou, Z., Tian, H., Wang, J.-S., et al. 2022, ApJ, 928, 98
Howard, R. A., Moses, J. D., & Vourlidas, A. 2008, SSRv, 136, 67
Kentischer, T. J., Bethge, C., Elmore, D. F., et al. 2008, Proc. SPIE, 7014, 701413
Kuhn, J. R., Lin, H., & Loranz, D. 1991, PASP, 103, 1097
Lemen, J. R., Title, A. M., Akin, D. J., et al. 2012, SoPh, 275, 17
Li, C., Fang, C., Li, Z., et al. 2022, SCPMA, 65, 289602
Li, J.-W., Li, H., Li, Y., et al. 2021, RAA, 21, 121
Lockwood, M. 2012, SGeo, 33, 503
Pesnell, W. D., Thompson, B. J., & Chamberlin, P. C. 2012, SoPh, 275, 3
Potts, H. E., & Diver, D. A. 2008, A&A, 492, 863
Pulkkinen, T. 2007, LRSP, 4, 1
Schwenn, R. 2006, LRSP, 3, 2
Seaton, D. B., Berghmans, D., Nicula, B., et al. 2013, SoPh, 286, 43
Song, Q., Wang, J.-S., Zhang, X., et al. 2022, ApJ, Under review
Wachter, R., & Schou, J. 2009, SoPh, 258, 331
Wang, Y., Bai, X., Liu, S., et al. 2019, SoPh, 294, 127
Withbroe, G. L. 1970, SoPh, 11, 42
Xu, G.-G., Zheng, S., Lin, G.-H., & Wang, X.-F. 2016, ApJ, 827, 137
Zhang, P., Hu, X., Lu, Q., et al. 2022, AdAtS, 39, 1